RESEARCH ARTICLE

ADVANCED FUNCTIONAL MATERIALS
www.afm-journal.de

High-Efficiency $Sb_2(S,Se)_3$ Solar Cells with New Hole Transport Layer-Free Back Architecture via 2D Titanium-Carbide Mxene

Hu Li, Limei Lin, Liquan Yao, Fengying Wu, Dong Wei, Guoliang Liu, Zhigao Huang, Shuiyuan Chen, Jianmin Li,* and Guilin Chen**

MXene, a class of 2D materials of metal carbide or nitride, has attracted a lot of attention recently due to its excellent optical and electrical properties. In this work, titanium-carbide MXene ($Ti_3C_2T_x$) is introduced as a back electrode in $Sb_2(S,Se)_3$ thin-film solar cells (FTO/CdS/$Sb_2(S,Se)_3$/MXene) for the first time, which displaces traditional carbon (C) and gold (Au) electrodes entirely. Impressively, thanks to its high conductivity, mild reflectivity, and flexible flake architecture, the MXene-based device performance outperforms typical C and Au electrodes by 153% and 77%, respectively. Specifically, the tunable work function of MXene and a beneficial Sb–O bond formed between $Sb_2(S,Se)_3$ and MXene efficiently suppress the recombination and enhance charge transport by enjoying the unique merit of the rich terminal groups of MXene. As a result, the best efficiency of 8.29% of MXene-based $Sb_2(S,Se)_3$ solar device is achieved, which represents the highest performance of noble metal and/or hole transport layer-free derived $Sb_2(S,Se)_3$ solar cells to date. This result has revealed that MXene is a feasible material to substitute the back electrode in Sb-based solar cells to reach high efficiency, low cost, and high stability.

1. Introduction

Recently, $Sb_2(S_xSe_{1-x})_3$ ($0 \le x \le 1$), a kind of single-phase compound belonging to antimony sulfur system materials, has attracted a lot of attention as a next-generation photovoltaic material in thin-film solar cells. It has a lot of advantages including high absorption coefficient (1.8×10^5 cm^{-1}), adjustable optical band gap (1.1–1.8 eV), abundant raw materials, and low temperature of growing crystal.[1–4] Over the past 6–7 years, tremendous efforts have been devoted to propelling the power conversion efficiency (PCE) of $Sb_2(S_xSe_{1-x})_3$ solar cells over 10%. However, it still lags far behinds that of the state-of-the-art thin-film solar cells such as copper indium gallium selenide and cadmium telluride.[5,6] The short carrier lifetime, complicated deep defects, and interface recombination are primarily responsible for poor device performance.[7,8] Among them, one of the crucial variables is severe recombination at the back contact interface, which is significantly dependent on the quality of the $Sb_2(S,Se)_3$/back contact materials (BCMs) interface. Hence, a careful selection of BCMs is necessary to fully realize the potential of $Sb_2(S,Se)_3$ solar cells.

Up to now, the BCMs for $Sb_2(S,Se)_3$ solar cells are mainly divided into two kinds including hole transport layer (HTL) and conductive electrode. For HTL, it can extract holes effectively with a suitable valence band maximum (VBM) and block electrons with a high conduction band minimum (CBM). One of the most successful HTLs is the organic Spiro-OMeTAD, which is fully exploited by the Chen group and achieves a PCE of 10% for $Sb_2(S,Se)_3$ solar cell.[9] However, the high cost and the instability of Spiro-OMeTAD are the most serious bottleneck toward its commercialization. Hence, some groups have been working on finding out new inorganic HTLs, for example, CuSCN, PbS, V_2O_5, and NiO_x, to enhance device stability.[10–14] But the low electrical conductivity of CuSCN and NiO_x partly pull down the performance of $Sb_2(S_xSe_{1-x})_3$ solar cells, and the toxicity of PbS and V_2O_5 will instigate eco-friendly anxiety. Another application of BCMs is the direct deposition of a conducting electrode on the bare surface of $Sb_2(S_xSe_{1-x})_3$, in which

---

H. Li, L. M. Lin, L. Q. Yao, F. Y. Wu, Z. G. Huang, G. L. Chen
Fujian Provincial Engineering Technology Research Center
of Solar Energy Conversion and Energy Storage
College of Physics and Energy
Fujian Normal University
Fuzhou 350117, China
E-mail: glchen@fjnu.edu.cn

H. Li, L. M. Lin, D. Wei, G. L. Liu, Z. G. Huang, S. Y. Chen, G. L. Chen
Fujian Provincial Collaborative Innovation Center for Advanced
High-Field Superconducting Materials and Engineering
Fuzhou 350117, China
E-mail: sychen@fjnu.edu.cn

J. M. Li
Key Laboratory of Artificial Micro- and Nano-structures
of Ministry of Education
and School of Physics and Technology
Wuhan University
Wuhan 430072, China
E-mail: ljmphy@whu.edu.cn

The ORCID identification number(s) for the author(s) of this article can be found under https://doi.org/10.1002/adfm.202110335.

DOI: 10.1002/adfm.202110335

the Au electrode with high conductivity and work function (WF, 5.1 eV) is dominated as BCMs in $Sb_2(S_xSe_{1-x})_3$ solar cell. By enjoying the preferred band alignment induced by high WF of Au, Chu and co-workers employed a vapor transport deposition way to refresh the recorded PCE of HTL-free $Sb_2(S,Se)_3$ solar cell to 8.17%.[15] It is justifiable to use Au electrodes on small-size samples, but it will contribute to high overall fabrication costs in solar cell technologies that rely on large-area devices. In addition, C has a WF close to that of gold, which is also regarded as a potential low-cost electrode material to replace Au and delivers a moderate PCE of ≈5% in $Sb_2(S,Se)_3$ solar cells.[16,17] However, the contact resistance between the C electrode and $Sb_2(S,Se)_3$ is large, which is primarily answerable for the lagging device performance. Besides, for another side of the back contact interface, the composition (S/Se ratio) of $Sb_2(S_xSe_{1-x})_3$ thin film will essentially affect its surface chemistry and energy level, which complicates the band alignment of the back contact interface of devices.[18,19] But, the reported WF of carbon and Au BCMs are relatively fixed, which will not meet the needs of the versatile back contact interface regulation. Therefore, it is urgent to develop green, stable, low-cost, and WF adjustable BCMs for the exploration of highly efficient $Sb_2(S,Se)_3$ solar cells.

MXene is an emerging 2D material, which has excellent physical and chemical properties such as conductivity, heat conduction, bandgap, photoelectric, mechanical, and thermodynamic properties.[20–25] It receives great attention in the field of energy storage and optoelectronic devices.[26,27] In particular, MXene shows a great application potential in the photovoltaic device by taking advantage of its high conductivity, adjustable WF, and stable structure.[28–32] For example, MXene can be used to modify the electron transfer layer and perovskite layer, or served as HTL for perovskite solar cells.[33–36] Another underexplored but remarkable characteristic of MXene is the flexible WF, which can be adjusted continuously from 1.6 to 6.25 eV by regulating the relative content of terminal groups (O–, F–, and OH-, etc.).[37] The above outstanding properties of MXene are crucial for back contact engineering in thin-film solar cells, however, the corresponding application in $Sb_2(S,Se)_3$ solar cells is rarely reported.

In this work, pure and uniform 2D MXene ($Ti_3C_2T_x$) nanoflakes are successfully synthesized and then coated on the rear surface of $Sb_2(S,Se)_3$ thin film by thermal spraying as a novel electrode, which is finally assembled into devices with FTO/CdS/$Sb_2(S,Se)_3$/MXene structure. Given the traits of high conductivity, flexible flake architecture structure, and excellent hole extraction efficiency of $Ti_3C_2T_x$, the relevant PCE of $Sb_2(S,Se)_3$ solar cell significantly outperforms the C and Au counterparts. We also make a detailed analysis of the interaction between $Sb_2(S,Se)_3$ and MXene, revealing that the negatively charged T_x group of MXene can be tightly attached and heal the sulfur-vacancy defect on $Sb_2(S,Se)_3$ surface, which effectively reduces the recombination and enhances the carrier transport at back interface. Further manipulation of the WF of MXene, which is expected to realize the band alignment coordination between MXene and $Sb_2(S,Se)_3$, resulting in a preferable arrangement of back contact energy levels and enhanced holes extraction.

2. Results and Discussion

2.1. Synthesis of 2D MXene and Spraying it as BCMs

In this work, as shown in the schematic diagram of **Figure 1**a,b, 2D MXene ($Ti_3C_2T_x$) is first synthesized by etching the Al layers out of the Ti_3AlC_2 MAXene phases using wet-chemical etchant (lithium fluoride (LiF)/hydrochloric acid (HCl)). For more details, please refer to the Experimental Section. As a result, a pure and highly c-oriented MXene product is obtained without any MAXene trace (Figure 1d). And the sharp and intensive peak of (002) indicates a high degree of crystallization of MXene.[38] A uniform MXene nanosheets with a lateral size of 400–500 nm is presented in SEM image of Figure S1a, Supporting Information. As expected, it is remarkedly distinguished from the lumpy morphology of its parent phase, attributing to the extraction of Al element in the block thoroughly during the ultrasonic stripping process (Figure S1b, Supporting Information). This uniformly lamellar structure is confirmed by transmission electron microscopy (TEM) image in **Figure 2**e. The corresponding selected area electron diffraction (SAED) pattern is also recorded in the inset, which shows a hexagonal symmetry structure and reflects the high crystallinity of MXene nanosheets.[39] And the correlated TEM mapping (Figure S2, Supporting Information) presents a homogenous composition distribution across the MXene nanosheet. As the optoelectrical property of MXene nanosheet is greatly dependent on its thickness, we measured the related metrics by atomic force microscope (AFM, Figure 2f). The thickness of MXene nanosheet is determined to be 1.15 nm, which is in line with that of monolayered MXene as previously reported.[40] X-ray photoelectron spectroscopy (XPS) analysis is carried out to ulteriorly detect the chemical composition of $Ti_3C_2T_x$ as shown in Figure S3a, Supporting Information, indicating the presence of all the elements of Ti, C, O, Cl, and F. There is a small amount of Cl, originating from the Cl-contained etchant, which has also been detected in previously reported work.[41] And the F and O elements are the terminal groups of MXene. We carefully inspect the high-resolution spectrum of C 1s, Ti 2p, and F 1s peaks to study the chemical bonding (Figure S3b–d, Supporting Information). Apart from the dominant peaks associated with the Ti–C bond of $Ti_3C_2T_x$, the chemical bonding between Ti atoms and T_x (O–, OH–, and F-) terminal groups are detected.[42] More detailed analysis can be found in Figure S3, Supporting Information. These manifest the high-quality bonding between Ti and C in the as-synthesized MXene, accompanied by rich terminal groups.[43] Raman spectra are used to further confirm the formation of pure MXene with rich functional groups (Figure S4, Supporting Information). A distinct sharp peak at 204 cm^{-1} is assigned to the out-of-plane vibration (A_{1g}) of Ti and C atoms, and the region 230–470 cm^{-1} represents in-plane (E_g) vibrations of surface groups attached to titanium atoms.[42] It is worth noting that the relatively wide Raman peaks may be induced by the coexistence of various surface terminating functional groups that affect the phonon dispersion of MXene. Moreover, the absence of a peak at 144 cm^{-1} indicates that MXene has not been oxidized to form titanium dioxide.[44] In brief, in terms of structure, morphology, and composition, the as-prepared MXene exhibits its superior features of pure phase,

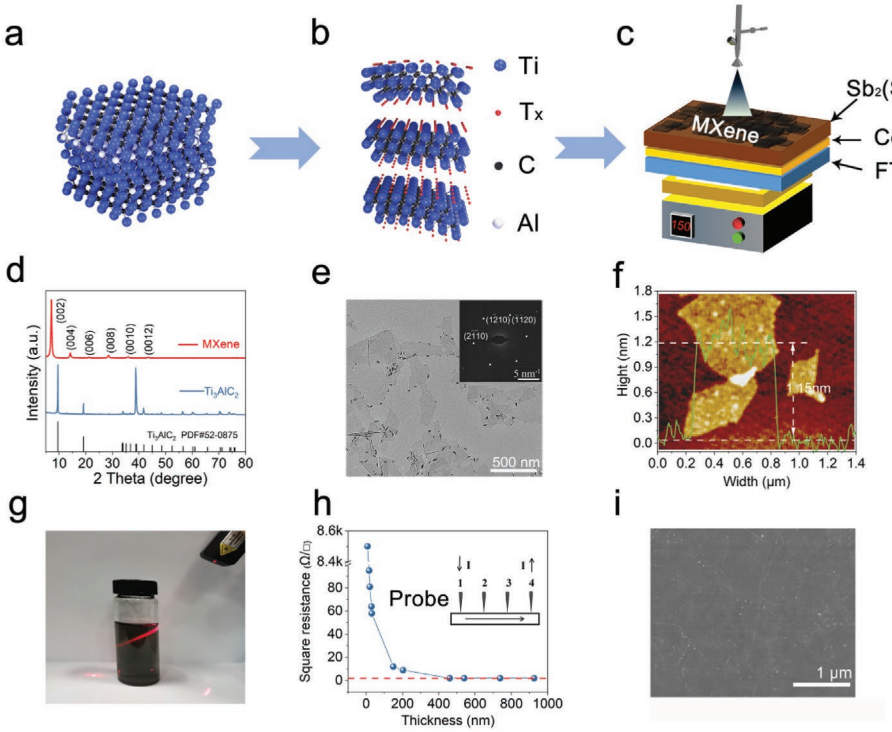

Figure 1. Schematic diagram of the etching process (i.e., stratification) for MXene layers. a) MAXene, b) MXene, and c) spraying deposition of MXene on FTO/CdS/$Sb_2(S,Se)_3$ substrate. Characterization of MXene layer. d) XRD patterns of MAXene and as-prepared MXene nanoflakes, e) TEM and SAED image (inset), and f) AFM topography image of single-layered MXene. Preparation and characterizations of MXene films. g) Dispersions of MXene in the water. h) Square resistance of the MXene layer varies with its thickness, in which the mean sheet resistance is based on ten independent test results, and i) SEM morphology of as-sprayed MXene layer.

high crystallinity, mono-layered architecture, and rich terminal groups, which lays a foundation for its versatile application in the photoelectric device.

To coat a high-quality MXene layer, the prerequisite is the achievement of a stable MXene solution, aiming to match it with the targeted substrates. Hence, we first test the dispersity of MXene in a wide range of solvents for 96 h (Figure S5, Supporting Information). Among these solvents, all the deionized water, alcohol, dimethylformamide, and dimethylsulfoxide lead to stable dispersions of MXene nanoflakes, while the methanol and acetone counterparts display an opposite direction. This can be explained by the strong correlation between surface tension, colloid concentration, boiling point, dielectric constant, and polarity in the various solvent properties.[45] Preferably, we select the low-cost and eco-friendly water as a dispersion medium to form a stable colloid solution in this work, which exhibits an obvious "Tyndall effect" (Figure 1g). And the long-term stability of this MXene ink is also verified after being stored for 40 days (Figure S6, Supporting Information). Sequentially, the water-based MXene solution is facilely deposited into a thin film by thermal spraying, which is efficient and low manufacturing cost as illustrated in Figure 1c. The conductivity, one of the most appealing characters of the as-coated MXene film, is further explored with the variation of its thickness by a four-point probe test (Figure 1h). The sheet resistance decreases dramatically from 8501 Ω/□ to 2 Ω/□ as the thickness of film increases from 7 nm to 460 nm, where the 460 nm is then selected as the optimal thickness. This tendency can be explained by the increased connection of MXene nanosheets with duration as shown in its morphology evolution during the spray process (Figure S7, Supporting Information). The surface morphology of the completed MXene film is exhibited in Figure 1h, displaying a highly uniform, smooth, and pore-free layer because of the ultrahigh-aspect-ratio of the MXene nanosheet and self-assembling process. Compared with the deep-dug superior conductivity, the unexplored mechanical flexibility is purposely tested in Figure S8, Supporting Information. After bending with 50 cycles, both the morphology and conductivity of the MXene coated on the flexible substrates are unscathed. This is connected to the high flexibility and adhesion of MXene nanoflakes which enables it to match well the substrates with different roughness. Such a high-quality MXene layer with few defects is entitled to an excellent carrier transport and collection ability, which is anticipated as promising BCMs in the $Sb_2(S,Se)_3$ solar cell.

2.2. The Basic Performance of MXene-Based $Sb_2(S,Se)_3$ Devices

With the excellent characteristic of the MXene layer displayed above, it is then deposited on the rear surface of the as-prepared $Sb_2(S,Se)_3$ layer by thermal spraying. This is the first application of MXene nanoflakes in of $Sb_2(S,Se)_3$ solar cell. As counterparts, two most popular electrode materials of C and gold are also used as BCMs in the same device structure of

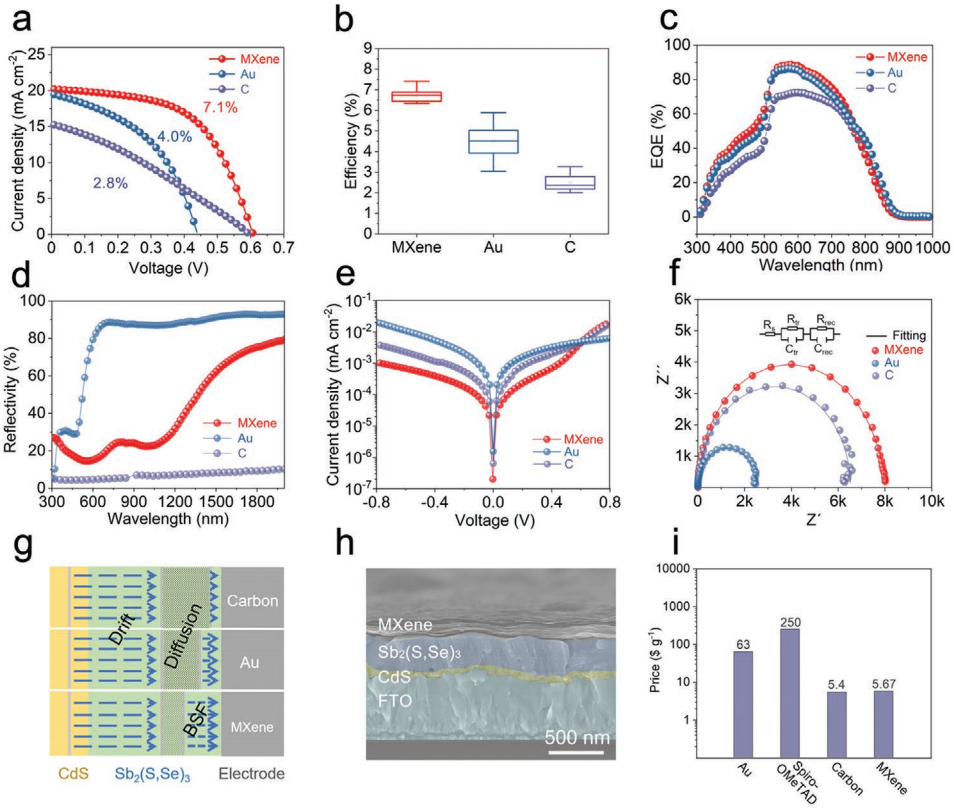

Figure 2. Device performance and analysis. a) The *J*–*V* curves, b) device efficiency statistics charts, and c) EQE spectra of $Sb_2(S,Se)_3$ thin-film solar cells with C, Au, and MXene electrodes, respectively. d) The reflection spectrum of C, Au, and MXene electrodes. e) Dark *J*–*V* characteristics and f) Nyquist plots of the typical $Sb_2(S,Se)_3$ thin-film solar cells. Inset: the equivalent electronic circuit model. g) Schematic diagram of electric field built with different electrodes. h) Cross-sectional SEM of FTO/CdS/$Sb_2(S,Se)_3$/MXene. i) Prices of various BCMs.

FTO/CdS/$Sb_2(S,Se)_3$/electrode. The typical current density–voltage (*J*–*V*) curves of devices with different electrodes are recorded in Figure 2a. It can be observed that the performance of MXene-based devices overwhelms that of C and Au-based device in all-around metrics of PCE, open-circuit voltage (V_{oc}), short-circuit current density (J_{sc}), and fill factor (FF). To further confirm the device difference as well as repeatability of different devices, the statistic boxplots of device parameters are exhibited in Figure 2b (PCE) and Figure S9, Supporting Information (V_{oc}, J_{sc}, and FF). All the device metrics illustrate that MXene BCMs renders a perfect back contact and then effectively improves device performance compared with the conventional C and Au BCMs.

As for J_{sc}, both MXene- and Au-based devices are found to have higher values thanks to their superior electrical conductivity and wonderful back contact. In contrast, a large number of pores are observed in the back contact interface of carbon-based $Sb_2(S,Se)_3$ solar cells (more details can be found in the cross-sectional morphology of its device in Figure S10, Supporting Information), due to the high viscosity of carbon paste. The resulted imperfect interface produces a large contact resistance, which pulls down both J_{sc} and FF. This is also verified by the external quantum efficiency (EQE) (Figure 2c), showing an inferior response of carbon-based devices compared with the MXene and Au counterparts in the whole spectrum. The identical device structure renders the same spectral response range independent of the diverse electrodes adopted, however, the maximum EQE of 70% for carbon based-device is observably lower than that of MXene and Au (about 90%). This can be explained by the fact that the high back contact resistance of the carbon case leads to a poor carrier collection efficiency in $Sb_2(S,Se)_3$ solar cells. On the other hand, the reflection of electrodes is important but often overlooked for improving the full utilization of incident light reached the back contact. Incomplete absorption of the $Sb_2(S,Se)_3$ film is noticed under its absorption band (800 nm) as shown in Figure S11, Supporting Information, attributing the too-thin absorb layer. Considering the trade-off between absorption and bulk recombination, the thickness of $Sb_2(S,Se)_3$ film is optimized to be 350 nm according to the previous work,[9] which inevitably penetrates over 5% (Figure S11, Supporting Information) light under its band edge and then decreases J_{sc} of the device. It is well known that most of the conventional metal electrodes have a high reflectivity under specific wavelength (i.e, Au: 500 nm; Ag: 300 nm) because the light with low frequency will be entirely reflected by electric field screening of a large amount of free electron.[46] Meanwhile, the smoothness of the metal surface is also contributed to such a high reflectivity. As the similar electrical property of MXene is possessed, its reflectivity is then examined in Figure 2d. It can be intuitively observed that MXene has a nonnegligible reflectivity (25%) in the visible region compared with that of Au (90%) and C (5%)

electrodes. To quantify it, we calculate the J_{sc} gain given the whole range of light is uniformly absorbed by $Sb_2(S,Se)_3$ layer (more detail can be found in Figure S12, Supporting Information). A net increased J_{sc} of 0.58 mA cm^{-2} is then obtained by enjoying the reflection of the MXene electrode. Therefore, the MXene electrode, with essential features of high conductivity and moderate reflectivity, enables the achievement of high current density and is qualified as a potential BCMs for $Sb_2(S,Se)_3$ solar cells.

In terms of V_{oc}, a parameter that reflects the device recombination is distinguished from various electrodes-based devices. The J–V test in the dark (Figure 2e) shows the lowest leakage current of 2×10^{-7} mA cm^{-2} in the MXene equipped device, indicating the reduced carrier combination and better rectification behavior. Generally, the leakage current here is the result of the Shockley–Read–Hall recombination of carriers in the depletion layer or interface. As the synthesis procedure of $CdS/Sb_2(S,Se)_3$ junction is identical, the relatively smallest leakage current of the MXene device can be ascribed to the formation of benign back contact interface compared with the C and Au counterparts. For further assessing the back contact of the devices, the Nyquist plots of the devices were employed (Figure 2f). The inset of Figure 2f exhibits the equivalent electronic circuit employed to fit the electrochemical impedance spectrum (EIS) impedance spectra. R_{rec} is the composite resistance at BCMs which is inversely proportional to the charge recombination rate of the device. The fitting results of R_{rec} with Au, C, and MXene electrodes are as follows: 2523, 6309, and 7837 Ω, respectively. The reason for the low R_{rec} of electrode Au may be explained by the possible penetration of Au vapor through the pinhole of $Sb_2(S,Se)_3$ layer during the deposition process. In contrast, both C and MXene electrode delivers a relatively large R_{rec}, which are attributed to favorable deposition strategies for those two electrodes. We will discuss them in the following section in the view of back contact morphology afterward.

Back surface field (BSF) is another critical factor for the carrier transportation and collection of devices, which should be drawn attention as various electrodes are adopted. To dig out more information about the BSF, capacitor–voltage (C–V) measurement is carried out under dark conditions (Figure S13, Supporting Information). The built-in voltage (V_{bi}) of the device is then deduced by fitting the straight-line portion of C^{-2}–V curves, outputting V_{bi} of 1.07, 1.02, and 0.86 V for MXene, Au, and carbon electrodes-based devices respectively. According to the typical $Sb_2(S,Se)_3$ device structure, the generated built-in electric field is composed of a PN junction field and BSF. Therefore, in the case of an identical preparation process of PN junction, the variation of V_{bi} is supposed to be derived from the different BSF induced with these three electrodes. Once the electrode with a high WF (MXene > Au > C, measured by Kelvins probe force microscopy (KPFM), Figure S14, Supporting Information) is contacted with p-type $Sb_2(S,Se)_3$, the large band bending between $Sb_2(S,Se)_3$ and electrode is formed, creating a wide BSF. As shown in the schematic diagram of BSF (Figure 2g), the MXene generates the largest BSF, which covers the most neutral region of $Sb_2(S,Se)_3$ and thus effectively improves the separation of photogenerated carriers. Such a perfect BSF impels photo-induced electrons away from the back surface and then reduces electron–hole recombination velocity. However, in the case of Au and C, the photogenerated holes near the $CdS/Sb_2(S,Se)_3$ interface need to travel a longer distance to reach the BSF region, which is easily combined with electrons in this diffusion process. Consequentially, a high value of V_{bi}, reflecting a large depletion region of the whole device, is positively correlated to the V_{oc}. And a prominent V_{oc} has been therefore observed in $Sb_2(S,Se)_3$ solar cells employing MXene electrode. It is worth mentioning that the V_{bi} of the Au electrode (1.02 V) overtop that of the carbon electrode (0.86 V), however, the V_{oc} of them shows a contradictory trend. This can be explained by the fact the Au vapor in the process of thermal evaporation will penetrate through any possible pin-hole in the $Sb_2(S,Se)_3$ layer, leading to an enlarged leakage current which is in line with the previous dark J–V test results.

In order to reveal the interface contact more visually, the morphology characteristics of the back contact are shown in Figure 2h and Figure S10, Supporting Information. Due to the hyperviscosity of carbon paste, the as-coated carbon electrode displays the roughest contact interface with large amounts of holes, which significantly affects the overall transport and collection of charge carriers and drag down the J_{sc} and FF of the device undoubtedly. In contrast, Au electrode is an ideal contact with low contact resistance for $Sb_2(S,Se)_3$ solar cell. But it can even penetrate through a few pinhole defects in $Sb_2(S,Se)_3$ layer, causing a sharp drop in the V_{oc} of device, which is consistent with the J–V, EIS, and C–V analyses. For the MXene BCMs, its preeminent feature of flexibility, which has been testified in the aforementioned spraying MXene layer, enables feasible adjusting of its deposition shape according to the fluctuation of the $Sb_2(S,Se)_3$ surface so that the contact is extremely tight. Combining with its high electrical conductivity, MXene leads to a low R_s of the device. More important, the MXene nanosheet with a large lateral size endows an excellent over-coverage of any possible pinholes in the $Sb_2(S,Se)_3$ layer, which remarkably reduces the shunt-path and then enhances V_{oc} of the device.

On top of that, the cost and element reserve of the BCMs are calculated and analyzed, as shown in Figure 2i. The prices of conventional BCMs, such as gold, Spiro-OMeTAD, and carbon paste are 63, 250, and 5.4 \$ g^{-1}, respectively, which are referred from the London Metal Exchange and shopping quotes.[47] The cost for lab synthesis of MXene is estimated to be ≈5.67 \$ g^{-1} according to the cost of raw materials used in the synthesis (more detail can be found in Table S1, Supporting Information). Gold has a high price and low reserve, especially when it is paired with Spiro-OMeTAD as BCMs, the total price will be even higher. As for carbon, its price is similar to that of MXene material, but the related device performance far lags than that of MXene. In brief, the MXene with brilliant features, such as high conductivity, large lateral size, low-cost, and flexible property, exhibits great potential in BCMs of $Sb_2(S,Se)_3$ solar cells.

2.3. The Interfacial Linking between $Sb_2(S,Se)_3$ and MXene

To reveal the intrinsic mechanism behind the remarkable efficiency enhancement, we carefully investigate the interfacial linking between $Sb_2(S,Se)_3$ and MXene. As a comparison, an ultra-thin MXene nanoflake (about 7 nm) is sprayed on

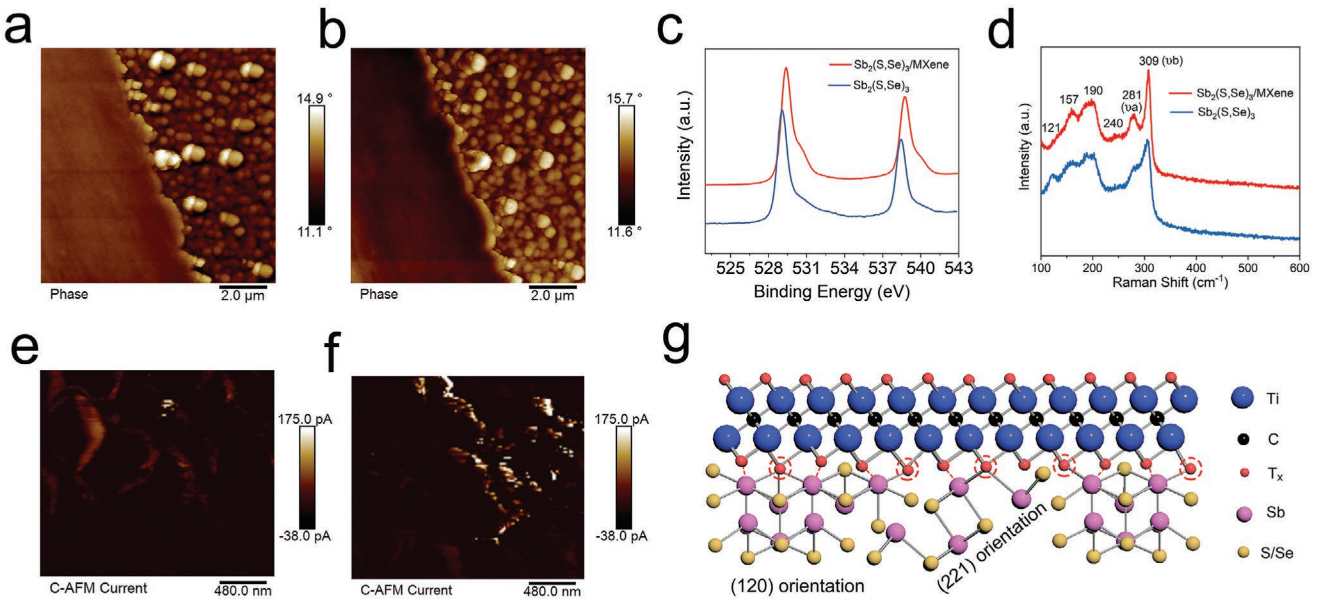

Figure 3. The interaction between Sb$_2$(S,Se)$_3$ and MXene. The EFM images with a) 2 and b) −2 V bias. c) The high-resolution XPS spectra of Sb 3d and d) Raman curves of Sb$_2$(S,Se)$_3$ with and without MXene. The c-AFM images of e) FTO/CdS/Sb$_2$(S,Se)$_3$ and f) FTO/CdS/Sb$_2$(S,Se)$_3$/MXene samples. g) The linking schematic diagram of the atomistic model of Sb$_2$(S,Se)$_3$ and MXene layers.

Sb$_2$(S,Se)$_3$ surface (Figure S15, Supporting Information) to exclude the interference by the thick MXene during the various interface tests. First, the surface charge of the pristine Sb$_2$(S,Se)$_3$ film was detected by electrostatic force microscopy (EFM). An EFM image applied bias voltage of ±2 V was concurrently acquired with the topographic image of Figure S16, Supporting Information, and these images are shown in **Figure 3**a,b. When a negative bias is applied, the probe polarization will induce a positive charge on the sample surface and vice versa.[48] Accordingly, the observed larger phase shift at negative bias voltage (−2 V) indicates that the surface charge of pristine Sb$_2$(S,Se)$_3$ film has the same polarity (positive) with the charge induced on its surface. As a result, the MXene nanoflakes are then electrostatically attached to Sb$_2$(S,Se)$_3$ surface, owing to the coupling between the oppositely charged Sb$_2$(S,Se)$_3$ surface and negatively charged functional groups (O−, F−, and OH−) of MXene, which creates a tight contact between them spontaneously. This strong electrostatic force is also confirmed by the binding energy (BE) shift of Sb 3d orbit. As shown in the XPS spectrum of Figure 3c, both Sb 3d5/2 and Sb 3d3/2 peaks of MXene attached Sb$_2$(S,Se)$_3$ sample show a slightly positive shift (≈0.34 and 0.31 eV) compared with that of pristine Sb$_2$(S,Se)$_3$ film. This positive shift of Sb 3d peaks might be attributed to the high electronegativity of T_x groups in MXene, suggesting the presence of strong interfacial interaction. In addition, a right shoulder of Sb 3d5/2 peaks, assigning to Sb–O bond, is carefully inspected after fitting the curve of the high-resolution Sb 3d peaks (Figure S17, Supporting Information). It can be found that the strength of the Sb–O bond increases after closely attaching MXene on the Sb$_2$(S,Se)$_3$ surface, which may be attributed to the chemically bonding between O- groups of MXene with surface-exposed Sb atoms of Sb$_2$(S,Se)$_3$ film.[49] In our experiment, the relatively large ratio of Sb/(S + Se) (1.64, Sb-rich) is deduced from the integral area of XPS peaks (Figure S18, Supporting Information). Such a potential chalcogen vacancy can be filled by foreign oxygen, according to the latest results conducted by Chen groups. They have reported that the substitutional defect O_S with low formation energy can passivate the dominant intrinsic donor V_S (defect localized state).[50] In order to further verify it, Raman tests are carried out to reveal this interaction between the surface V_S defect and MXene for defect passivation. As shown in Figure 3d, the dominant Raman bands at 190, 281, and 309 cm^{-1} along with three feeble weak peaks at 121, 157, and 240 cm^{-1} are assigned to Sb$_2$(S,Se)$_3$. Particularly, two dominant peaks at 281 and 309 cm^{-1} correspond to antisymmetric and symmetric stretching vibrations υ_a and υ_s (Sb–S), respectively.[51,52] A closer inspection of these two modes found that with MXene coupling, the intensity of peak corresponding to symmetric stretching (υ_s) gained its intensity. It indicates that there are fewer sulfur vacancies on Sb$_2$(S,Se)$_3$ surface with MXene according to the previous defect study by Raman.[53] And the striking narrowing of wide peak positions at 281 and 309 cm^{-1} also verifies the effective sulfur-vacancy passivation after MXene modification. Such a defect healing strategy can be explained by the fact that the negative T_x groups in MXene, especially the O group, will act as a sharing functional group and bond with the unpaired Sb atoms in Sb$_2$(S,Se)$_3$ (e.g., Sb–O). Furthermore, to access the accelerated charge transport and the suppressed interfacial charge recombination loss by MXene modification, we performed the conductive-AFM (c-AFM) image at 2 V bias (Figure 3e,f), and the related surface morphology was concurrently recorded in Figure S19a,b, Supporting Information. With the attachment of MXene, no obvious morphologic change of Sb$_2$(S,Se)$_3$ is observed compared with the pristine one due to the ultra-thin and flexible features of MXene nanoflakes. As depicted in Figure 3f, the MXene-covered area of Sb$_2$(S,Se)$_3$ has a larger photocurrent across grain boundaries when it is illuminated by a 633 nm laser, demonstrating an excellent charge transfer ability. This is due to the high conductivity and flexibility of MXene film, which enables it to make wonderful contact with $Sb_2(S,Se)_3$ film. To further reveal this contact, the possible Sb atoms exposed on the $Sb_2(S,Se)_3$ surface is analyzed and categorized as following two forms: a) breaking Sb–S bond and forming a comparably high concentration of V_S due to its low formation energy, supporting by the fact that the annealing of $Sb_2(S,Se)_3$ thin film is conducted under chalcogen-free atmosphere (N_2) in our technical route; b) the terminals of trigonal SbS_3 and square SbS_5 pyramids are considered as possible pairing sites with foreign anions. Consequentially, MXene with rich terminal groups T_x enables a strong interaction with the exposed Sb atoms and forms a sound chemical bonding, which is illustrated in Figure 3g. Two typical crystal planes, (221) and (120), in the crystallized $Sb_2(S,Se)_3$ thin films are adopted in the atomistic model, which are referred from its X-ray diffraction (XRD) patterns (Figure S20, Supporting Information).[9] The crystalline defects and dangle bonds attached to the $Sb_2(S,Se)$ surface will be remarkably alleviated after forming a chemical bridge using a T_x linker. Therefore, such a surface trap-mediated strategy can reduce the nonradiative charge recombination for achieving high-efficiency $Sb_2(S,Se)_3$ solar cells.

2.4. Band Alignment Engineering of Back Contact

As discussed above, the $Sb_2(S,Se)_3$ layer is praiseworthy for its robust bandgap engineering, which can manipulate the VBM and CBM of $Sb_2(S,Se)_3$ by simply regulating the S/Se ratio.[54] This in turn causes a complex band alignment at the back contact interface. Hence seeking BCMs with an adjustable WF is of prime importance to the construction of a preferred back contact interface. Different from the conventional Au and C electrodes, the emerging 2D MXene possesses an outstanding regulation capability of its WF via modifying the terminal functional group. Here, as illustrated in **Figure 4**a, the as-deposited MXene layer is suffered from UV-ozone treatments for 30 min in order to regulate its WF. As shown in the KPFM test of Figure 4b, the WF of the pristine MXene electrode is higher than that of the Au electrode, which is reflected in the improved device performance as discussed above. Even more encouraging, the ozone-treated one exhibits a slightly increased WF compared with the control one. As shown in the Raman spectrum (Figure 4c), after ozone treatment, the characteristic vibration peak located 394 cm^{-1} (assigning to OH group) obviously moves to 378 cm^{-1} (assigning to O group), while the other characteristic peak positions are almost unchanged (maintains the structure of MXene).[42]

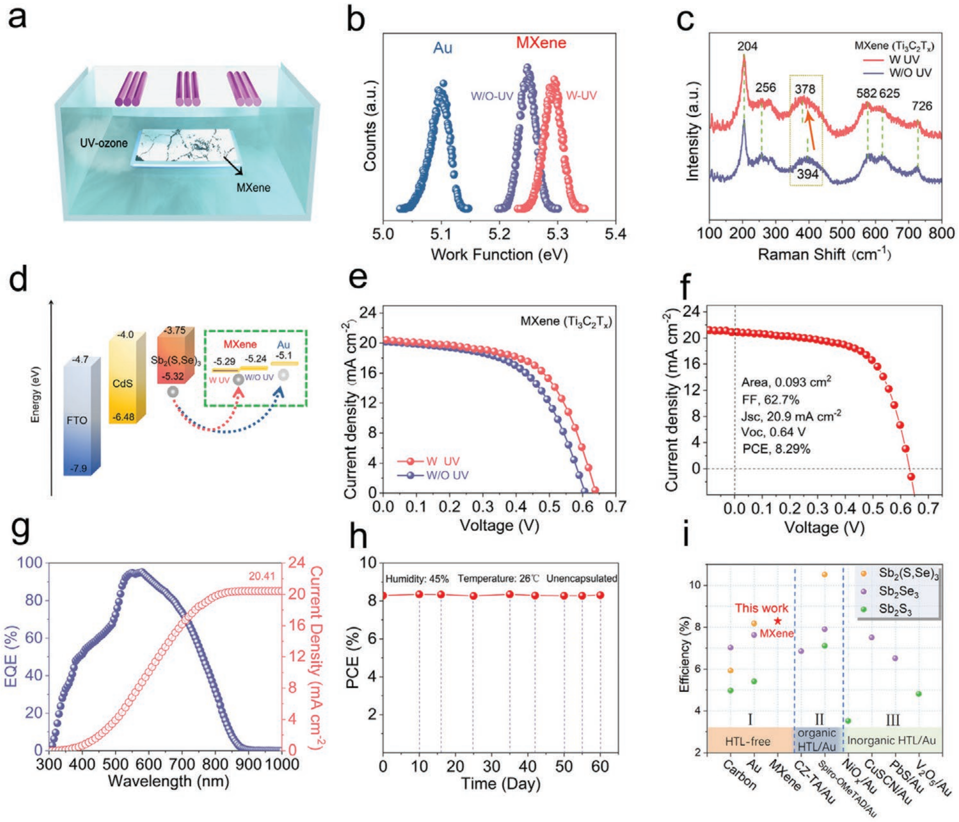

Figure 4. Performance of ozone modified devices. a) Schematic representation of UV-ozone treatment on MXene film. b) The WF of Au and MXene with and without ozone treatment detected by KPFM. c) Raman spectrums of MXene films with and without ozone treatment. d) The band alignment diagram of the $Sb_2(S,Se)_3$ device. e) The *J–V* curves of $Sb_2(S,Se)_3$ devices using MXene BCMs with and without ozone treatment. Performance and stability of champion devices. f) The *J–V* curve and g) EQE spectra of the best $Sb_2(S,Se)_3$ thin-film solar cells with ozone-treated MXene electrode. h) The relationship curve of PCE of the best device and exposes time. i) The champion efficiency for $Sb_2(S_xSe_{1-x})_3$ solar cells with different BCMs (regions I, II, and III represent HTL-free, organic HTL/Au, and inorganic HTL/Au, respectively).

This composition change is also confirmed by the XPS test as shown in Figure S21, Supporting Information. After ozone treatment, all the peaks of XPS assigned to MXene remain unchanged except the relative strength of O/F in comparison with the pristine MXene (Figure S3, Supporting Information). The ozone exposure remarkably increases the intensity of O 1s peaks and decreases that of F 1s peaks, meaning that the F group is partially replaced by the O group. Such an increased content of O- functional groups will render an enhanced WF of MXene film according to the reported experience of band level engineering by manipulating the functional groups of MXene,[28] which agrees well with the above result of KPFM. It is also worth noticing that the square resistance of the ozone-treated MXene film (2.4 Ω/□) is similar to that of the pristine one (2.0 Ω/□), as shown in Figure S22 in Supporting Information. In brief, the ozone treatment can facilely engineer the WF of MXene without any change in its bulk properties such as structure and conductivity.

As more O-terminal groups are formed after ozone treatment, the higher WF of MXene will be obtained. To reveal the carrier transportation at the back contact interface equipped with various electrodes, the band energy level of $Sb_2(S,Se)_3$ is first recorded by ultraviolet photoelectron spectroscopy (UPS). The VBM, CBM, and E_g of the as-prepared $Sb_2(S,Se)_3$ layer are derived to be −5.32, −3.75, and 1.57 eV, respectively (more calculation details can be found in Figure S23a–c, Supporting Information). Finally, combining with the WF with different electrodes, the band alignment of $Sb_2(S,Se)_3$ planar solar cells is then sketched in Figure 4d, where the band energy level data of FTO and CdS are referred from the literature.[55] Compared with Au and pristine MXene electrodes, the WF of ozone-treated MXene is found to be more close to the VBM of $Sb_2(S,Se)_3$ which observably reduces the hole injection barrier as well as nonradiative recombination at the $Sb_2(S,Se)_3$/MXene interface compared with the other two counterparts. Thus, such a preferred band alignment delivers a lower contact resistance at its back contact interface and promotion of hole collection efficiency. Hence, MXene exhibits tremendous potential as BCMs in the $Sb_2(S,Se)_3$ solar cell by enjoying its robust WF engineering.

To assess the impact of band alignment engineering, the device performances are tested by the J–V in typical $Sb_2(S,Se)_3$ devices with the pristine and ozone-treated MXene electrodes, as shown in Figure 4e. And the device parameters of the representative devices are shown in Table S2, Supporting Information, indicating a remarkable improvement of PCE from 7.1% to 7.8% after ozone treatment. Such facile engineering of the back contact interface leads to an increase in V_{oc} and FF and consequentially boosts PCE. To further verify the reproductivity of these two devices, the statistical comparison of J_{sc}, V_{oc}, FF, and PCE are shown in Figure S24f–j, Supporting Information. The J_{sc} values are almost the same, while both V_{oc} and FF are slightly improved, ascribing to the enhanced efficiency of hole extraction and reduced carrier recombination by the preferred band alignment at the back contact interface. In a word, the favorable modification of MXene by ozone treatment makes it more suitable for $Sb_2(S,Se)_3$ solar cells.

In order to demonstrate the superiority of the ozone-treated MXene electrode, we measure the J–V curve of the related champion device (Figure 4f). It delivers a PCE of 8.29%, with J_{sc} of 20.9 mA cm^{-2}, V_{oc} of 0.64 V, and FF of 62.7%. Typically, the device displays a negligible hysteresis, confirmed by the almost same J–V curves measured under both reverse- and forward-scan directions (Figure S25, Supporting Information). The EQE test result along with the integral curve corresponding to the champion device are given in Figure 4g. It shows an absorption value of up to 95% at the highest point, which is comparable to that of the state-of-the-art Antimony-based device with Spiro-OMeTA/Au BCMs.[9] It indicates that the ozone-treated MXene electrode is conducive to carrier separation and transportation and improves the overall efficiency of the device, which is considered one of the ideal BCMs. However, there is still a large margin of improvement of EQE response in the short-(300–500 nm) and long-(650–850 nm) wavelength, mainly ascribing to the severe parasitic absorption of CdS and bulk recombination of $Sb_2(S,Se)_3$ absorber, which should be improved by reducing the thickness or widening the band-gap of the CdS buffer layer, and optimizing the preparation process for absorber with less defects. The normalized PCE of the best device (unencapsulated) as a function of the expose time in ambient conditions with 45% humidity, 26 °C room temperature is shown in Figure 4h. After 60 days, the device exhibits negligible changes in PCE, indicating superior device stability with MXene BCMs. We also summarize the maximum efficiency of different BCMs of current $Sb_2(S_xSe_{1-x})_3$ thin-film solar cells as shown in Figure 4i. We can find that the MXene-derived device in our work is the first time to join the club of over 8% efficiency using the noble metal and/or organic-free BCMs for $Sb_2(S_xSe_{1-x})_3$ solar cells.[10–13,15,56–64] This back contact engineering strategy, via the novel, stable, and eco-friendly BCMs of MXene electrode, enables to achieve a low-cost and full-inorganic $Sb_2(S,Se)_3$ solar cell with high efficiency.

3. Conclusion

In conclusion, we introduce a low-cost and green 2D MXene ($Ti_3C_2T_x$) as BCMs in the $Sb_2(S,Se)_3$ solar cell by spraying route. The MXene-based $Sb_2(S,Se)_3$ solar cell delivers a more prominent device performance than the conventional carbon and Au electrodes, attributing to the tight contact induced by its flexible nanoflakes architecture, electrostatically attachment to $Sb_2(S,Se)_3$ surface, as well as formed a beneficial chemical bridge bond of Sb–O at $Sb_2(S,Se)_3$/MXene interface. Furthermore, by modifying the terminal functional group, the WF of MXene may be tailored to meet the need for complicated band alignment at the back contact interface of the $Sb_2(S,Se)_3$ solar cell. As a result, the desired band arrangement of back contact is established, which significantly improves hole collecting efficiency. Finally, a champion PCE of 8.29% (V_{oc} of 0.64 V, J_{sc} of 20.9 mA cm^{-2}, and FF of 62.7%) is achieved in the novel configuration of FTO/CdS/$Sb_2(S,Se)_3$/MXene, which is the highest reported PCE so far for noble-metal and/or HTL $Sb_2(S,Se)_3$ solar cells. This research provides a potential MXene electrode for the versatile back contact engineering of the $Sb_2(S,Se)_3$ device, pointing to a promising future for low-cost planar $Sb_2(S,Se)_3$ solar cells.

4. Experimental Section

Chemical: MAXene (Ti_3AlC_2, 400 mesh, Shandong Xiyan New Material Technology Co. LTD), LiF (AR, Aladdin), HCl (36–38%, Sinopharm), thiourea (CH_4N_2S, AR, Sinopharm), cadmium nitrate tetrahydrate ($Cd(NO_3)_2{\cdot}4H_2O$, AR, Sinopharm), ammonium hydroxide ($NH_3{\cdot}H_2O$, 25–28%, Sinopharm), cadmium chloride hemipentahydrate ($CdCl_2{\cdot}2.5H_2O$, AR, Sinopharm), methanol (CH_3OH, AR, Macklin), potassium antimony (III) L(+)-tartrate hemihydrate ($C_4H_4KO_7Sb{\cdot}0.5H_2O$, AR, Sinopharm), sodium thiosulfate pentahydrate ($Na_2S_2O_3{\cdot}5H_2O$, AR, Sinopharm), selenourea (CH_4N_2Se, 99.97%, Alfa), carbon electrode paste (C, 99%, Shanghai Materwin New Materials Co. LTD), and gold (Au, 99.999%, Beijing Dream Material Technology Co. LTD).

Fabrication of PN Junction: The device structure of the $Sb_2(S,Se)_3$ planar solar cell was FTO/CdS/$Sb_2(S,Se)_3$/MXene. To build a PN junction of CdS/$Sb_2(S,Se)_3$, the FTO glasses were first ultrasonically cleaned with deionized water, acetone, and ethanol in sequence for 60 min. The surface of the FTO was treated with UV-ozone for 20 min to decompose organic contaminants. Second, an n-type CdS layer with 65 nm was deposited on the FTO by the chemical bath deposition method according to the previous report.[17] After deposition, a post-treatment of CdS was conducted by spin coating of $CdCl_2$ absolute solution (0.05 g $CdCl_2$ was soluble in 10 mL methanol) at 3000 rpm for the 30 s. Then, the CdS substrate was annealed in air at 380 °C for 5 min, followed by cooling to room temperature naturally. Afterward, the hydrothermal method was adopted for the deposition of $Sb_2(S,Se)_3$ as an absorber layer according to the previously reported recipe.[9] The $Sb_2(S,Se)_3$ film was synthesized by using $Na_2S_2O_3{\cdot}5H_2O$, $KSbC_4H_4O_7{\cdot}0.5H_2O$, and selenourea as S, Sb, and Se sources, respectively. In brief, 0.12 g selenourea, 20 mM $KSbC_4H_4O_7{\cdot}0.5H_2O$ and 80 mM $Na_2S_2O_3{\cdot}5H_2O$ were added into a Teflon tank (100 mL) of an autoclave that contained 80 mL of ultrapure water, which was then heated at 135 °C for 2 h. After the hydrothermal reaction, the sample was washed with ultrapure water and dried on a hotplate at 70 °C for 10 min under atmospheric pressure. Finally, the film was annealed on a hotplate at 350 °C for 10 min in a glove box filled with N_2 (1–1.5 mbar) to enhance its crystallinity.

Preparation of the Electrodes: To synthesize 2D MXene nanoflakes, 0.5 g of Ti_3AlC_2 powder was first immersed into a mixture solution of 10 mL of 9 M HCl under magnet stir for 10 min. Then 1 g of LiF was added and mixed at 45 °C in a water bath for 24 h. Sequentially, the sediment was collected by centrifugation at 3500 rpm for 5 min. Afterward, 1 M hydrochloric acid was used to rinse the product three times to remove the LiF which was not completely reacted. Once the pH of the supernatant was about 6, the cleaning process was completed. Sequentially, the precipitate was ultrasonically dispersed into 20 mL of deionized water for 90 min in the presence of nitrogen. After centrifuge was done at 3500 rpm for 40 min, the upper homogeneous solution was collected as the target solution.

The prepared MXene solution was deposited directly on the $Sb_2(S,Se)_3$ layer by thermal spraying as a back electrode, which can be seen in Figure 1c. The distance between the spray gun and substrate was fixed to 12 cm, while the spray process lasts 30 s with the substrate temperature of 150 °C. A mask with an aperture area of 0.093 cm^2 was applied to define the effective device area. For the carbon electrode counterpart, a graphite paste was coated on the surface of $Sb_2(S,Se)_3$ thin films as back contact using a brush, and sequentially baked at 120 °C for 15 min. Next, the carbon electrodes were covered by silver paste and heated at 80 °C for 10 min. For the Au case, a 200 nm of Au thin film was also deposited for comparison by thermal evaporation under a pressure of 5.0×10^{-4} Pa.

Devices Characterizations: The structural properties of the MAXene and MXene were characterized by XRD (D/Max-rA). The microstructure was observed using high-resolution field emission scanning electron microscopy attached with energy dispersive spectroscopy (SU-8010). The WF of films was obtained by using KPFM (Bruker Dimension Icon), which could also obtain AFM, EFM, and c-AFM data through different test modules. Among them, the light source used in c-AFM test was 633 nm green light with a power of 1 mW. The surface composition was characterized by XPS (Shimadu, AXIS SUPRA+). The *J–V* curves and *C–V* spectra of the solar cells were characterized using a Keithley 4200-SCS semiconductor characterization system equipped with an AAASAN-EI ELECTRIC solar simulator (XES-40S1). The solar simulator illumination intensity was calibrated by a monocrystalline silicon reference cell (PV Measurements, PVM959) calibrated by the National Renewable Energy Laboratory (NREL). The measurement of impedance spectra was tested at 1 Hz to 1 MHz by Zennium (Zahner) electrochemical workstation in dark conditions. UPS was performed by PHI 5000 VersaProbe III with He I source (21.22 eV) under an applied negative bias of 9.0 V. UV–vis absorption spectra (Shimadzu, UV-2450) was carried out for the optical property. The EQE of the devices was performed by a solar cell quantum efficiency measurement system (Model QEX10).

Supporting Information

Supporting Information is available from the Wiley Online Library or from the author.

Acknowledgements

This work was supported by the National Natural Science Foundation of China (Grant no. 61974028) and Fujian Normal University (FNU) Training Program of Innovation and Entrepreneurship for Undergraduates (cxxl-2019135, 2019140, and 2019143). The authors also would like to thank Dr. Kong (Huaibei Normal University, China) for XPS test support and helpful discussions.

Conflict of Interest

The authors declare no conflict of interest.

Author Contributions

G.-L.C. and S.-Y.C. supervised the project at the Fujian Normal University of China while J.-M.L. supervised the work at the Wuhan University of China. H.L. and G.-L.C. conceived the original concept and designed the experiments. H.L. fabricated the devices and conducted the photovoltaic and optical characterization and analysis, while H.L. and F.-Y.W. carried out the MXene preparation and analysis. L.-L.L. and L.-Q.Y. conducted the SEM and AFM specimen preparation and performed the characterization and data analysis. H.L., D.W., and S.-Y.C. discussed and analyzed the dates of c-AFM and EFM. G.-L.C. conducted the figure modification and adjustment. H.L. and G.-L.C. co-wrote the manuscript. J.-M.L., D.W., S.-Y.C., and Z.-G.H. revised the manuscript with all authors commenting on the manuscript.

Data Availability Statement

The data that supports the findings of this study are available in the supplementary material of this article.

Keywords

back contact, band alignment engineering, MXene, $Sb_2(S,Se)_3$ solar cells

Received: October 12, 2021
Revised: October 29, 2021

[1] Y. Yin, C. Wu, R. Tang, C. Jiang, G. Jiang, W. Liu, T. Chen, C. Zhu, *Sci. Bull.* **2019**, *64*, 136.
[2] C. Chen, Y. Zhao, S. Lu, K. Li, Y. Li, B. Yang, W. Chen, L. Wang, D. Li, H. Deng, F. Yi, J. Tang, *Adv. Energy Mater.* **2017**, *7*, 1700866.
[3] G. X. Liang, Y. D. Luo, S. Chen, R. Tang, Z. H. Zheng, X. J. Li, X. S. Liu, Y. K. Liu, Y. F. Li, X. Y. Chen, Z. H. Su, X. H. Zhang, H. L. Ma, P. Fan, *Nano Energy* **2020**, *73*, 104806.
[4] Y. Cao, X. Zhu, H. Chen, X. Zhang, J. Zhou, Z. Hu, J. Pang, *Sol. Energy Mater. Sol. Cells* **2019**, *200*, 109945.
[5] P. Jackson, R. Wuerz, D. Hariskos, E. Lotter, W. Witte, M. Powalla, *Phys. Status Solidi RRL* **2016**, *10*, 583.
[6] M. G. Panthani, J. M. Kurley, R. W. Crisp, T. C. Dietz, T. Ezzyat, J. M. Luther, D. V. Talapin, *Nano Lett.* **2014**, *14*, 670.
[7] C. Chen, J. Tang, *ACS Energy Lett.* **2020**, *5*, 2294.
[8] Y. Cao, X. Zhu, J. Jiang, C. Liu, J. Zhou, J. Ni, J. Zhang, J. Pang, *Sol. Energy Mater. Sol. Cells* **2020**, *206*, 110279.
[9] R. Tang, X. Wang, W. Lian, J. Huang, Q. Wei, M. Huang, Y. Yin, C. Jiang, S. Yang, G. Xing, S. Chen, C. Zhu, X. Hao, M. A. Green, T. Chen, *Nat. Energy* **2020**, *5*, 587.
[10] K. Li, S. Wang, C. Chen, R. Kondrotas, M. Hu, S. Lu, C. Wang, W. Chen, J. Tang, *J. Mater. Chem. A* **2019**, *7*, 9665.
[11] C. Chen, L. Wang, L. Gao, D. Nam, D. Li, K. Li, Y. Zhao, C. Ge, H. Cheong, H. Liu, H. Song, J. Tang, *ACS Energy Lett.* **2017**, *2*, 2125.
[12] L. Zhang, C. Jiang, C. Wu, H. Ju, G. Jiang, W. Liu, C. Zhu, T. Chen, *ACS Appl. Mater. Interfaces* **2018**, *10*, 27098.
[13] X. Jin, Y. Yuan, C. Jiang, H. Ju, G. Jiang, W. Liu, C. Zhu, T. Chen, *Sol. Energy Mater. Sol. Cells* **2018**, *185*, 542.
[14] J. Zhang, R. Kondrotas, S. Lu, C. Wang, C. Chen, J. Tang, *Sol. Energy* **2019**, *182*, 96.
[15] Y. Pan, X. Hu, Y. Guo, X. Pan, F. Zhao, G. Weng, J. Tao, C. Zhao, J. Jiang, S. Chen, P. Yang, J. Chu, *Adv. Funct. Mater.* **2021**, *31*, 2101476.
[16] O. A. Jaramillo-Quintero, M. E. Rincón, G. Vásquez-García, P. K. Nair, *Prog. Photovolt.* **2018**, *26*, 709.
[17] L. Yao, L. Lin, H. Liu, F. Wu, J. Li, S. Shui, Z. Huang, G. Chen, *J. Mater. Sci. Technol.* **2020**, *58*, 130.
[18] C. Wu, L. Zhang, H. Ding, H. Ju, X. Jin, X. Wang, C. Zhu, T. Chen, *Sol. Energy Mater. Sol. Cells* **2018**, *183*, 52.
[19] Y. Cao, C. Liu, J. Jiang, X. Zhu, J. Zhou, J. Ni, J. Zhang, J. Pang, M. H. Rummeli, W. Zhou, H. Liu, G. Cuniberti, *Sol. RRL* **2021**, *5*, 2000800.
[20] M. Xu, S. Lei, J. Qi, Q. Dou, L. Liu, Y. Lu, Q. Huang, S. Shi, X. Yan, *ACS Nano* **2018**, *12*, 3733.
[21] J. Wang, Z. Cai, D. lin, K. Chen, L. Zhao, F. Xie, R. Su, W. Xie, P. Liu, R. Zhu, *ACS Appl. Mater. Interfaces* **2021**, *13*, 32495.
[22] M. Shi, P. Xiao, J. Lang, C. Yan, X. Yan, *Adv. Sci.* **2020**, *7*, 1901975.
[23] S. Ahn, T. Han, K. Maleski, J. Song, Y. Kim, M. Park, H. Zhou, S. Yoo, Y. Gogotsi, T. Lee, *Adv. Mater.* **2020**, *32*, 2000919.
[24] K. Li, M. Liang, H. Wang, X. Wang, Y. Huang, J. Coelho, S. Pinilla, Y. Zhang, F. Qi, V. Nicolosi, Y. Xu, *Adv. Funct. Mater.* **2020**, *30*, 2000842.
[25] D. Xu, Z. Li, L. Li, J. Wang, *Adv. Funct. Mater.* **2020**, *30*, 2000712.
[26] S. Zhang, H. Ying, B. Yuan, R. Hu, W. Han, *Nano-Micro Lett.* **2020**, *12*, 78.
[27] P. Lu, J. Wu, X. Shen, X. Gao, Z. Shi, M. Lu, W. W. Yu, Y. Zhang, *Adv. Sci.* **2020**, *7*, 2001562.
[28] Z. Yu, W. Feng, W. Lu, B. Li, H. Yao, K. Zeng, J. Ouyang, *J. Mater. Chem. A* **2019**, *7*, 11160.
[29] Y. Yang, H. Lu, S. Feng, L. Yang, H. Dong, J. Wang, C. Tian, L. Li, H. Lu, J. Jeong, S. M. Zakeeruddin, Y. Liu, M. Gratzel, A. Hagfeldt, *Energy Environ. Sci.* **2021**, *14*, 3447.
[30] A. Agresti, A. Pazniak, S. Pescetelli, A. D. Vito, D. Rossi, A. Pecchia, M. A. Maur, A. Liedl, R. Larciprete, D. V. Kuznetsov, D. Saranin, A. D. Carlo, *Nat. Mater.* **2019**, *18*, 1228.
[31] X. Chen, W. Xu, N. Ding, Y. Ji, G. Pan, J. Zhu, D. Zhou, Y. Wu, C. Chen, H. Song, *Adv. Funct. Mater.* **2020**, *30*, 2003295.
[32] C. Zhang, L. Cui, S. Abdolhosseinzadeh, J. Heier, *InfoMat* **2020**, *2*, 613.
[33] Z. Zhang, Y. Li, C. Liang, G. Yu, J. Zhao, S. Luo, Y. Huang, C. Su, G. Xing, *Small* **2020**, *16*, 1905896.
[34] A. D. Vito, A. Pecchia, M. A. Maur, A. D. Carlo, *Adv. Funct. Mater.* **2020**, *30*, 1909028.
[35] T. Chen, G. Tong, E. Xu, H. Li, P. Li, Z. Zhu, J. Tang, Y. Qi, Y. Jiang, *J. Mater. Chem. A* **2019**, *7*, 20597.
[36] X. Chen, W. Xu, N. Ding, Y. Ji, G. Pan, J. Zhu, D. Zhou, Y. Wu, C. Chen, H. Song, *Adv. Funct. Mater.* **2020**, *30*, 2003295.
[37] M. Khazaei, M. Arai, T. Sasaki, A. Ranjbar, Y. Liang, S. Yunoki, *Phys. Rev. B* **2015**, *92*, 075411.
[38] L. Yang, C. Dall'Agnese, Y. Dall'Agnese, G. Chen, Y. Gao, Y. Sanehira, A. K. Jena, X. Wang, Y. Gogotsi, T. Miyasaka, *Adv. Funct. Mater.* **2019**, *29*, 1905694.
[39] V. Kamysbayev, A. S. Filato, H. Hu, X. Rui, F. Lagunas, D. Wang, R. F. Klie, D. V. Talapin, *Science* **2020**, *369*, 979.
[40] L. Ding, Y. Wei, L. Li, T. Zhang, H. Wang, J. Xue, L. Ding, S. Wang, J. Caro, Y. Gogotsi, *Nat. Commun.* **2018**, *9*, 155.
[41] C. Liu, M. Miao, Y. Li, J. Zhang, S. Cao, X. Feng, *ACS Appl. Mater. Interfaces* **2018**, *10*, 44787.
[42] A. Sarycheva, Y. gogotsi, *Chem. Mater.* **2020**, *32*, 3480.
[43] Z. Li, P. Wang, C. Ma, F. Igbari, Y. Kang, K. L. Wang, W. Song, C. Dong, Y. Li, J. Yao, D. Meng, Z. K. Wang, Y. Yang, *J. Am. Chem. Soc.* **2021**, *143*, 2593.
[44] H. Fu, V. Ramalingam, H. Kim, C. Lin, X. Fang, H. N. Alshareef, J. He, *Adv. Energy Mater.* **2019**, *9*, 1900180.
[45] K. Maleski, V. N. Mochalin, Y. Gogotsi, *Chem. Mater.* **2017**, *29*, 1632.
[46] M. Bartek, J. H. Correia, R. F. Wolffenbuttel, *J. Micromech. Microeng.* **1999**, *9*, 162.
[47] C. Jiang, J. Zhou, R. Tang, W. Lian, X. Wang, X. Lei, H. Zeng, Z. Chang, W. Tang, T. Chen, *Energy Environ. Sci.* **2021**, *14*, 359.
[48] B. Son, J. Park, O. Kwon, *Polymers* **2021**, *13*, 1258.
[49] T. Honma, R. Sato, Y. Benino, T. Komatsu, V. Dimitrov, *J. Non-Cryst. Solids* **2000**, *272*, 1.
[50] Z. Cai, C. M. Dai, S. Chen, *Sol. RRL* **2020**, *4*, 1900503.
[51] R. Parize, T. Cossuet, O. Chaix-Pluchery, H. Roussel, E. Appret, V. Consonni, *Mater. Des.* **2017**, *121*, 1.
[52] A. Maiti, S. Chatterjee, A. J. Pal, *ACS Appl. Energy Mater.* **2020**, *3*, 810.
[53] W. Lian, C. Jiang, Y. Yin, R. Tang, G. Li, L. Zhang, B. Che, T. Chen, *Nat. Commun.* **2021**, *12*, 3260.
[54] K. Li, Y. Lu, X. Ke, S. Li, S. Lu, C. Wang, S. Wang, C. Chen, J. Tang, *Sol. RRL* **2020**, *4*, 2000220.
[55] W. Wang, X. Wang, G. Chen, L. Yao, X. Huang, T. Chen, C. Zhu, S. Chen, Z. Huang, Y. Zhang, *Adv. Electron. Mater.* **2018**, *5*, 1800683.
[56] X. Wang, R. Tang, C. Jiang, W. Lian, H. Ju, G. Jiang, Z. Li, C. Zhu, T. Chen, *Adv. Energy Mater.* **2020**, *10*, 2002341.
[57] D. Liu, R. Tang, Y. Ma, C. Jiang, W. Lian, G. Li, W. Han, C. Zhu, T. Chen, *ACS Appl. Mater. Interfaces* **2021**, *13*, 18856.
[58] K. Li, C. Chen, S. Lu, C. Wang, S. Wang, S. Wang, Y. Lu, J. Tang, *Adv. Mater.* **2019**, *31*, 1903914.
[59] J. Han, S. Wang, J. Yang, S. Guo, Q. Cao, H. Tang, X. Pu, B. Gao, X. Li, *ACS Appl. Mater. Interfaces* **2020**, *12*, 4970.
[60] H. Deng, Y. Zeng, M. Ishaq, S. Yuan, H. Zhang, X. Yang, M. Hou, U. Farooq, J. Huang, K. Sun, R. Webster, H. Wu, Z. Chen, F. Yi, H. Song, X. Hao, J. Tang, *Adv. Funct. Mater.* **2019**, *29*, 1901720.
[61] B. Ríos-Ramirez, P. K. Nair, *Phys. Status Solidi A* **2018**, *215*, 1800479.
[62] Z. Chen, G. Chen, *Sol. Energy* **2020**, *201*, 323.
[63] D. B. Li, X. Yin, C. R. Grice, L. Guan, Z. Song, C. Wang, C. Chen, K. Li, A. J. Cimaroli, R. A. Awni, D. Zhao, H. Song, W. Tang, Y. Yan, J. Tang, *Nano Energy* **2018**, *49*, 346.
[64] L. Guo, B. Zhang, S. Ranjit, J. Wall, S. Saurav, A. J. Hauser, G. Xing, L. Li, X. Qian, F. Yan, *Sol. RRL* **2019**, *3*, 1900225.